ACCSCIENCE PUBLISHING

International Journal of Bioprinting

ACCEPTED PAPER · MAIN TEXT

Silk fibroin–reinforced bioink for high-fidelity 3D printing and tissue regeneration

Article ID: IJB026260265

Citation: Zhai X, Hu M, Chen Y, *et al*. Silk fibroin–reinforced bioink for high-fidelity 3D printing and tissue regeneration. *Int J Bioprint*. 2026. doi: 10.36922/IJB026260265

AccScience Publishing
RESEARCH ARTICLE
Volume X Issue X (2026)
doi: 10.36922/IJB026260265

Silk fibroin–reinforced bioink for high-fidelity 3D printing and tissue regeneration

Running title: Silk fibroin for DLP 3D bioprinting

Xinrang Zhai[1,2], Miner Hu[3], Yao Chen[1], Linran Song[1], Xihao Pan[4], Xianzhu Zhang[5], Wei Dong[2]*, Jianjun Ma[1*], and Wei Wei[1,6]*

[1] Department of Orthopedics, Center for Regenerative and Aging Medicine, International Institutes of Medicine, the Fourth Affiliated Hospital, International School of Medicine, Zhejiang University, Yiwu, Zhejiang 322000, China
[2] School of Chemistry and Chemical Engineering, Nanjing University of Science and Technology, Nanjing, Jiangsu 210094, China
[3] Department of Cardiology, Children's Hospital, Zhejiang University School of Medicine, National Clinical Research Center for Children and Adolescent's Health and Diseases, Hangzhou, Zhejiang 310000, China
[4] Liangzhu Laboratory, Zhejiang University, 1369 West Wenyi Road, Hangzhou 311121, China
[5] Department of Sports Medicine of the First Affiliated Hospital, Zhejiang University School of Medicine, Hangzhou, Zhejiang 310000, China
[6] Zhejiang Key Laboratory of Precision Diagnosis and Treatment for Lung Cancer, Yiwu, Zhejiang 322000, China

***Corresponding authors:**
Wei Dong (dongwei@njust.edu.cn)
Jianjun Ma (sealteam@zju.edu.cn)
Wei Wei (zjewwei@zju.edu.cn)

Citation: Zhai X, Hu M, Chen Y, *et al*. Silk fibroin–reinforced bioink for high-fidelity 3D printing and tissue regeneration. *Int J Bioprint.* 2026. doi: 10.36922/IJB026260265

Received: April 14, 2026
1st revised: June 22, 2026
2nd revised: July 9, 2026
Accepted: July 17, 2026
Published online: July 17, 2026

Abstract

Digital light processing (DLP) 3D printing is a technology for additive fabrication of objects layer by layer, guided by digital light patterns. It effectively addresses the demand for complex geometries and is widely adopted in the biological field. However, traditional macromolecular bioinks still suffer from printing inaccuracies due to light scattering and runaway free-radical reactions. Herein, we introduce silk fibroin (SF) into the conventional PEGDA/CSMA bioink to enhance the precision of DLP 3D printing. The incorporation of SF achieves a significant improvement in mechanical property (alcohol-induced β-sheet formation increased the compressive modulus from 9.5 kPa to 208.1 kPa) and anti-swelling performance (volume swelling ratio from about 366.1% to 144.6%) of cell-free PEGDA/CSMA/SF hydrogel via alcohol treatment, meeting the enhanced mechanical requirements and addressing the commonly neglected issue of geometric deformation of 3D-printed hydrogels caused by swelling in moist environments. Ethanol treatment induces SF β-sheet structure formation and reduces PEGDA/CSMA/SF hydrogel pore size (from about 78.3 μm to 23.6 μm), thereby enhancing the hydrogel network crosslinking. The PEGDA/CSMA/SF bioink possesses antibacterial potential, inhibiting *E. coli* by about 41.3% and *S. aureus* by about 45.8% within 12 h *in vitro*. The porous scaffolds are printed with a designed PEGDA/CSMA/SF bioink and effectively accelerate defect repair in rat full-thickness skin wound models (about 19.1% of the untreated control group). Histological analysis reveals that the PEGDA/CSMA/SF hydrogel scaffold promotes angiogenesis and collagen deposition, upregulates VEGFA expression, and downregulates TNF-α expression. The straightforward approach of introducing SF into traditional bioinks represents a promising strategy for DLP 3D printing in tissue regeneration.

Keywords: 3D printing; Silk fibroin; High precision; Anti-swelling; Wound repair

1. Introduction

Three-dimensional (3D) printing is a revolutionary additive manufacturing technology [1,2]. This technology employs digital slicing software to discretize 3D models into a series of thin layers, then precisely prints and deposits the materials layer by layer until it ultimately transforms a virtual design into a physical object [3,4]. It can fabricate objects with highly complex geometries that would be prohibitively expensive to produce with traditional manufacturing technologies. In the field of biomedical engineering, digital light processing (DLP) 3D printing is spearheading technological innovation owing to its unrestrained customizability, high precision, and minimal time investment [5,6]. Currently, numerous studies employing DLP 3D printing technology for biomaterial design have emerged [7-9]. By incorporating active components such as medicines and cells, printing inks can be engineered to deliver enhanced therapeutic effects or enable other customized functions [10,11].

Bioinks used for DLP 3D printing are typically photoresponsive synthetic or modified natural macromolecular compounds [12,13]. Poly(ethylene glycol) diacrylate (PEGDA) is regarded as a predominant synthetic polymer for 3D printing bioinks, owing to its superior biocompatibility and tunable physical properties [14]. However, its inherent lack of bioactivity restricts PEGDA to a role as a passive carrier or structural support [15]. Therefore, PEGDA-based constructs typically require the incorporation of bioactive components to facilitate tissue repair. Chitosan (CS) is a cationic polysaccharide derived from chitin, considered as an effective skin repair material due to the antibacterial activity, hemostasis, and immunomodulatory [16,17]. CS is commonly functionalized with methacrylic anhydride (MA) to impart photocrosslinking ability for DLP 3D printing [18]. Drawing on reported relevant works [19,20], an optimal MA grafting degree eliminates CS's dependence on weak-acid protonation for dissolution by consuming amino groups, while simultaneously preserving its antibacterial efficacy and its potential to accelerate wound healing.

Nevertheless, inherent limitations arising from light scattering and runaway free-radical polymerization prevent the printed construct from achieving the original designed dimensional fidelity [21]. Therefore, various photoabsorbers and free-radical inhibitors are being explored to

address this issue. For example, He et al. synthesized curcumin-Na to suppress dimensional deviation in high-fidelity 3D printing via photoabsorption and free-radical inhibition [22]. Ma et al. introduced a biomacromolecule additive by modifying the (N-(2-aminomethyl)-4-(4-(hydroxymethyl)-2-methoxy-5-nitrosophenoxy) butanamide) molecule onto chondroitin sulfate to avoid cytotoxicity and enhance 3D printing precision [23]. The vast majority of research on DLP 3D printing focuses on improving printing precision or enhancing the efficacy of biological repair. A critical yet frequently overlooked issue in 3D-printed hydrogels is their tendency to swell rapidly [24]. Even when printed with high fidelity, hydrogels tend to absorb water and rapidly expand in moist environments, leading to deviations from the intended geometry. It poses challenges for specific applications, such as cell-loaded hydrogel systems.

SF is a natural polymeric protein extracted from silkworm cocoons, regarded as a valuable biomaterial owing to its exceptional biocompatibility, superior mechanical properties, controllable biodegradability, and facile modification [25,26]. Fei et al. explored an apoptotic vesicles-loaded SF/sodium alginate hydrogel to promote pulp regeneration by stimulating capillary lumen formation [27]. Wu et al. reported injectable glycidyl methacrylate-modified SF peptide nanofiber hydrogel composite scaffolds that promote cartilage regeneration [28]. Notably, SF can undergo gelation via a free-radical reaction in the presence of enzymes or catalysts [29]. Numerous studies on SF-containing photosensitive hydrogels demonstrate that SF does not completely arrest polymerization, unlike conventional inhibitors [30]. It suggests that moderate free radical scavenging capacity may curb runaway polymerization during 3D printing without entirely halting the free radical reaction. Further, the physicochemical properties of SF can be orchestrated by its β-sheet structure, which can be readily induced by physical stimuli, such as organic solvents and cyclic freeze-thaw cycles [31,32]. Therefore, the strategy to prevent excessive swelling is to impart a more stable hydrogel chemical structure through inducing SF β-sheet formation.

Here, we incorporated SF into the PEGDA/CSMA bioink and leveraged its limited free-radical binding capacity to enhance the fidelity of DLP 3D printing. We also induced SF β-sheet formation using alcohol to improve mechanical properties and anti-swelling capacity. The free radical-scavenging capacity of SF was verified to suppress runaway polymerization in 3D

printing. We assessed the antibacterial activity and biocompatibility of the bioink hydrogels *in vitro*. Further, hydrogel scaffolds were printed using the SF-containing PEGDA/CSMA bioink to promote repair of rat skin defects, and the therapeutic effects were evaluated using immunohistochemical and immunofluorescence staining.

2. Materials and methods

2.1. Materials

Silk was purchased from Zhejiang Xingyue Biotechnology CO., LTD. Chitosan (CS, degree of deacetylation ⩾ 95%, weight-average molecular weight: ~550 kDa) and 2,2-Diphenyl-1-picrylhydrazyl (DPPH) were provided by Macklin. Polyethylene glycol diacrylate (PEGDA, Mw: ~1000 Da), sodium carbonate (Na_2CO_3), sodium bicarbonate ($NaHCO_3$), and lithium bromide (LiBr) were purchased from Aladdin. Methacrylic anhydride (MA) was obtained from Sigma-Aldrich. Lithium phenyl-2,4,6-trimethylbenzoyl phosphinate (LAP) was purchased by Haining Jurassic Bio-tech company Ltd. Hydrogen peroxide (H_2O_2) was supplied by Zhejiang Hannuo Chemical Co., Ltd. Luria-Bertani broth (LB) and LB nutrient agar were purchased from Hope Bio-Technology Co., Ltd. Cell counting Kit-8 (CCK-8), Calcein/PI Cell Viability/Cytotoxicity Assay Kit, and Hydrogen Peroxide Content Assay Kit were bought from Beyotime.

2.2. Preparation of SF

Aqueous SF was prepared according to the published protocol [33]. Briefly, cocoon samples (5 g) were fragmented into small sections and subjected to a 30-minute boiling process in 2 L of Na_2CO_3 (0.02 M) aqueous solution to remove sericin. The extracted SF fibers were washed three times with preheated deionized water (~70 °C) and dried in an oven overnight. The dried fibers were dissolved in a 9.3 M LiBr solution at 60 °C for four hours and dialyzed against deionized water for 3 days. Then, the rough SF solution was further purified by centrifugation (9,000 rpm, 4 °C, 20 min). The obtained SF solution was concentrated to ~10% w/v and stored at 4 °C for subsequent experiments.

2.3. Preparation of CSMA

CSMA was synthesized according to our reported literature [34]. Firstly, CS (1 g) was dissolved in 100 mL of 1% acetic acid. MA (1 mL) was added to the solution at 60 ℃, and the mixture was stirred for 6 h. The obtained solution was neutralized with 10% $NaHCO_3$ and dialyzed against deionized water for 3 days. The final product was obtained by lyophilization and stored at 4 °C.

2.4. Preparation of bioinks

The PEGDA/CSMA/SF bioink formula is 7% PEGDA, 1% CSMA, 2% SF, and 0.25% LAP. All other bioinks mentioned in this paper were prepared with the relevant components at the same concentrations as the PEGDA/CSMA/SF bioink.

2.5. Characterization

^{1}H Nuclear Magnetic Resonance (^{1}H-NMR) spectrum of CSMA was obtained by an AV-300 NMR spectrometer (Bruker, 400 MHz). The chemical structures were also analyzed by Fourier transform infrared (FTIR) spectroscopy (Vertex 70, Bruker, Germany) in the 4000-400 cm-1 region. The microstructures of the hydrogels were observed using a ZEISS SIGMA 500 scanning electron microscope (SEM).

2.6. Rheological tests

We conducted rheological tests using the Anton Paar MCR302 rheometer with the OMINICURE LED UV light source (365 nm, 35 mW/cm^2). The intersection point of the storage modulus (G') and loss modulus (G") curves was regarded as the gelation point.

2.7. Swelling and degradation performance

A lyophilized hydrogel (m_0) was immersed in 5 mL PBS solution (37 ℃), and the weights were recorded as m_s at the required time. The swelling ratio was calculated as follows:

$$Swelling\ ratio = \frac{m_s - m_0}{m_0} \times 100\% \quad (1)$$

The degradation behavior was assessed by measuring the mass of the original hydrogel (m_g) and that of the hydrogel immersed in 5 mL PBS solution (37 ℃) at a pre-designed time (m_t).

The degradation degree was calculated as follows:

$$Mass\ remaining = \frac{m_t}{m_g} \times 100\% \quad (2)$$

2.8. Anti-swelling tests

Considering the impact of swelling on the geometric shape of the 3D printed hydrogels, we adopted the volume swelling ratio to evaluate the swelling resistance. The original hydrogel volumes were recorded as V_0. The volumes of hydrogels treated with alcohol and rehydrated were marked as V_t. The effect of alcohol treatment on the original hydrogel volumes and the anti-swelling effect of treated hydrogels was calculated as follows:

$$Volume\ expansion\ ratio = \frac{V_t}{V_0} \times 100\% \quad (3)$$

2.9. Mechanical tests

A universal test machine (MTS) was employed for the compressive tests. The stress-strain curves were obtained by compressing the hydrogels (10 mm in diameter, 2 mm in height) at a rate of 1mm/min. The compressive modulus was derived from the slope of the linear region between 10% and 20 % strain.

2.10. Antibacterial performance

The *Escherichia coli* (*E. coli*) and *Staphylococcus aureus* (*S. aureus*) were co-cultured with the hydrogels and SF solution in Luria-Bertani (LB) solution at 37 ℃ (initial OD = 0.03, 600 nm). We measured the OD values at different co-cultured times to assess the antibacterial effect of the biomaterials. After 12 h incubation, we diluted the above bacterial suspension 10^6 times, and spread 50 μL bacterial dilution evenly on the LB nutrient agar plates. The bacterial colony counts were observed to further evaluate the antibacterial efficacy after 12 h incubation at 37 ℃.

2.11. Biocompatibility experiments *in vitro*

Rat bone marrow stromal cells (BMSCs) (from Procell Life Science & Technology Co., Ltd) were selected for biocompatibility experiments and cultured with complete medium (10 % fetal bovine serum, 1 % penicillin–streptomycin in low glucose Dulbecco's modified Eagle's medium). PEGDA/CSMA and PEGDA/CSMA/SF bioinks are sterilized at 121℃ for 8 min.

Sterilized bioinks (5 μL) were added to a 96-well plate, and cured with 365 nm UV for 20 s. About 10^5 mL^{-1} BMSCs (100 μL) are co-cultured with the hydrogels at 37 ℃ and 5 % CO_2. We conducted CCK-8 staining and measured the OD values (450 nm) to assess the cell viability. Additionally, about 10^5 mL^{-1} BMSCs (1 mL) were cultured with 50 μL of cured bioink, and Live/Dead assay images were obtained using an inverted fluorescent microscope to evaluate cytocompatibility.

2.12. Free radical scavenging

2,2-Diphenyl-1-picrylhydrazyl (DPPH) is widely used to assess the free radical-scavenging capacity of materials, owing to its stable free radical character and distinct color change upon reduction. We added 200 μL of PEGDA/CSMA precursor, PEGDA/CSMA hydrogel, PEGDA/CSMA/SF hydrogel, or SF solution to 5 mL of DPPH solution (250 μM in 95 % ethanol) and stirred the mixture at 37 ℃ for 6 h. We measured the OD at 520 nm using a microplate reader to evaluate free radical-scavenging capability. Additionally, we evaluated the H_2O_2 scavenging capacity of the bioink hydrogels and the SF solution. 200 μL PEGDA/CSMA precursor, PEGDA/CSMA hydrogel, PEGDA/CSMA/SF hydrogel, or SF solution was added into 5 mL H_2O_2 solution (1mM), and the Hydrogen Peroxide Content Assay Kit measured the H_2O_2 scavenging efficiency.

2.13. DLP 3D printing

The adopted bioink formula was 7% PEGDA, 1% CSMA, 2% SF, and 0.25% LAP. We chose the EFL-BP86 DLP 3D printer equipped with a 405 nm UV source, a thermostatic system, and a 25 μm high-precision digital micromirror device chip for the next 3D printing experiments. The digital 3D models were saved as Stereolithography (STL) files and uploaded to the 3D printer. The printing parameters were set to a printing thickness of 100 μm, a light intensity of 10 mW/cm^2, and a single-layer exposure time of 5 s. After printing, the printouts were washed with deionized water to remove uncured inks.

2.14. Animal experiments

All animal procedures were performed in accordance with the guidelines approved by the Zhejiang University Ethics Committee (Ethical NO. ZJU202550988). Sprague-Dawley rats

(male, 200-250 g) were subjected to general anesthesia with Zoletil-50 (40 mg/kg). The rats' dorsal hair was shaved, and the skin was disinfected with povidone-iodine. Two full-thickness skin defects (10 mm in diameter) were created on the back. In the PEGDA/CSMA and PEGDA/CSMA/SF hydrogel groups, the hydrogel precursor was injected into the skin wound and in situ cured under 365 nm UV irradiation for 20 s. The printed bioink scaffolds were implanted into the skin defects in the PEGDA/CSMA/SF scaffold group. An equal volume of PBS was injected into the defect to serve as the control group. We performed daily observations of the wound healing. After 14 days, the rats were euthanized, and the skin tissues were collected for further investigation.

2.15. Histological analysis

The skin samples were fixed in the 4% paraformaldehyde solution for 1 day. After gradient dehydration, the skin tissues were embedded in paraffin and subsequently sectioned into 4-μm-thick slices. We performed Hematoxylin-Eosin (H&E) and Masson's trichrome staining according to standard protocols. Moreover, immunohistochemical staining for CD31 and immunofluorescence staining for TNF-α (Tumor Necrosis Factor-α) and VEGF (Vascular Endothelial Growth Factor) were performed to assess the therapeutic effect on the wound. All stained slices were imaged using a digital pathology slide scanner.

2.16. Statistical analysis

All experiments were conducted at least three times independently, and the quantitative data were exhibited as mean ± standard deviation (SD). The significance between the two groups was analyzed using two-tailed Student’s t-tests. Multiple comparisons were performed using Tukey’s post hoc test and one-way analysis of variance (ANOVA) (GraphPad Prism 9.0). *$p < 0.05$, **$p < 0.01$, and ***$p < 0.001$ indicate statistical significance, and ns indicates no significance.

3. Results and discussion

First, the CSMA macromonomer was synthesized by grafting methacrylic groups onto the CS macromolecular chains via amidation. We analyzed the chemical structure of the prepared

CSMA using ^{1}H-NMR spectroscopy. As shown in **Fig. 1a**, the peaks a and b of protons at 5.41 and 5.71 ppm (ascribed to conjugated vinyl groups) were observed, demonstrating that the methacrylic groups were successfully grafted onto CS molecular chains. The signal of peak c at about 2.02 ppm was attributed to the residual acetyl group protons of CS. The grafting degree of MA was calculated as 37% from the ratio of the integral area of peak a to one-third of that of peak c. In addition, a 2% CSMA + 0.25% LAP solution was irradiated with 365 nm UV light, and the mixture solidified within 20 s (Fig. 1b), further verifying that the designed modified photosensitive CS-based bioink was successfully prepared. We also studied the chemical structure of the adopted bioinks using FTIR spectra (**Fig. 1c**). In the spectrum of PEGDA, the peaks at 2881, 1724, 1640, and 1104 cm^{-1} were assigned to -CH_2-, C=O, C=C, and C-O-C stretching vibrations [35]. The characteristic peaks at 1620 cm^{-1} (C=O stretching vibration, amide I band) and 1056 cm^{-1} (C-O-C bridge symmetric stretching) were also observed in the CSMA spectrum [34]. In the FTIR spectra of SF, the characteristic peak at 1650 cm^{-1} (amide I) was ascribed to the C=O stretching vibration, 1526 cm^{-1} (amide II) was attributed to N-H bending vibration, and 1244 cm^{-1} (amide III) was owing to the C-N stretching vibration. The wide band around 3300 cm^{-1} was attributed to O-H and N-H stretching vibrations [36]. We further analyzed the secondary structure of SF through the amide I band (1590-1710 cm^{-1}). The second-derivative spectra were calculated, and the deconvolution curve was obtained using a resolution enhancement factor of 2.2 and a full width at half maximum of 20.0 cm^{-1}. We used Origin software for peak fitting with the Gauss function, and calculated each secondary structure content by the percentage of the sub-spectrum integral area (β-sheets 41.82 %, random coils 23.7 %, α-helices 18.3 %, and β-turns 16.46%) (**Fig. 1d**). Besides, we investigated the rheology of the bioinks. As displayed in **Fig. 1e**, the storage modulus (G') of PEGDA/CSMA/SF rapidly increased after UV irradiation, and became equal to the slowly growing loss modulus (G") at 2.1 s. It was indicated that the PEGDA/CSMA/SF bioink exhibited rapid cure, with polymerization beginning within 2.1 seconds under UV irradiation. The rapid photo-polymerization characteristic of PEGDA/CSMA/SF was key to achieving high efficiency in 3D printing. Moreover, as an indicator of its mechanical strength, it was found that the storage modulus of PEGDA/CSMA/SF was higher than that of PEGDA/CSMA (**Fig. 1f**). This was evidence that SF participates in the construction of hydrogel networks, which contributed to

the mechanical property strengthening. We also assessed the swelling ratio and degradation behaviors of bioink hydrogels. As shown in **Fig. 1g**, PEGDA/CSMA and PEGDA/CSMA/SF hydrogels reached the swelling equilibrium in 60 min. The equilibrium swelling ratio of PEGDA/CSMA was about 1737%, and that of PEGDA/CSMA/SF was about 783%. It was explained that the freeze-drying process before the swelling experiment increased the content of the SF β-sheet structure. The degradation of PEGDA/CSMA reached about 20.6%, and that of the PEGDA/CSMA/SF hydrogel was about 33.6% on the 14th day (Fig. 1h). These results confirmed the reliability of the bioink raw materials.

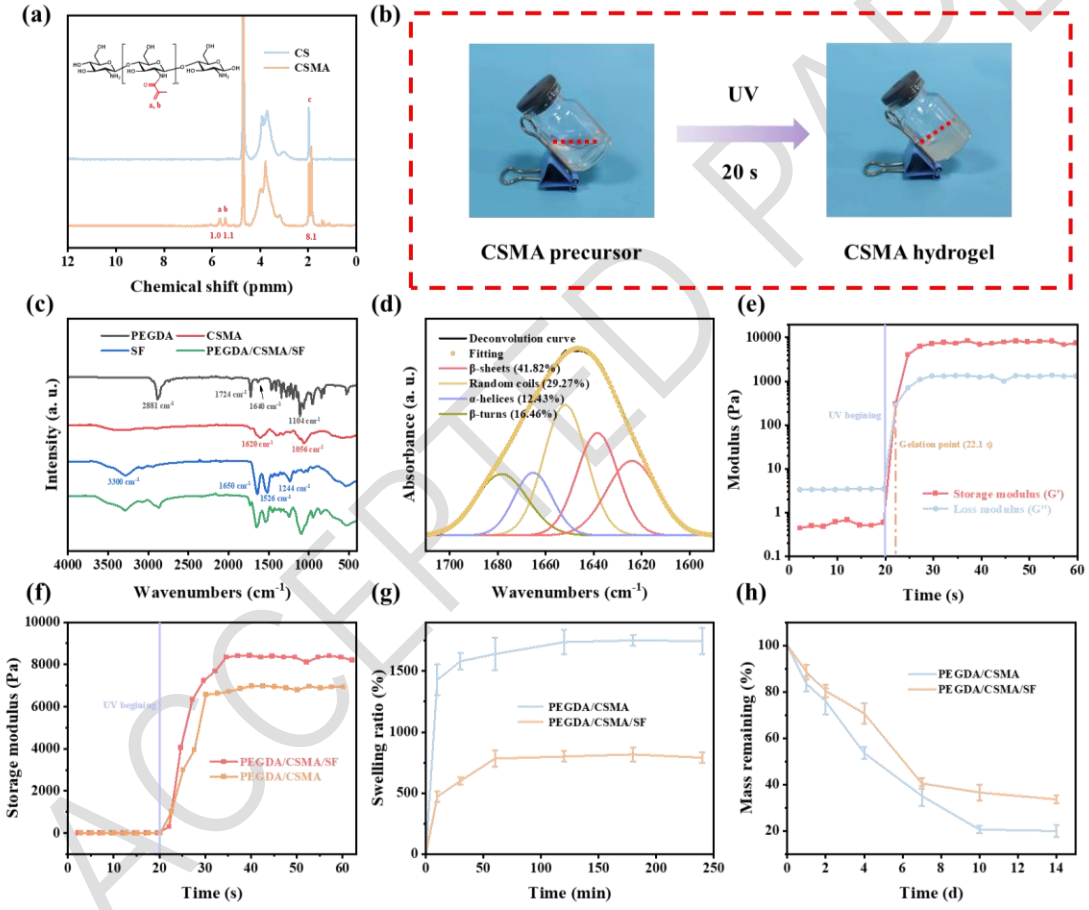

Figure 1. **The physicochemical properties of the bioinks**. ^{1}H-NMR spectroscopy of chitosan and CSMA **(a)**. CSMA gelation after UV irradiation **(b)**. FTIR spectrum of the bioink raw materials **(c)**. The quantitative analysis of the SF amide I band **(d)**. Rheology of PEGDA/CSMA/SF **(e)**. The storage modulus of PEGDA/CSMA and PEGDA/CSMA/SF **(f)**. Swelling ratio **(g)** and degradation performance **(h)** of PEGDA/CSMA and PEGDA/CSMA/SF.

There is still a challenge for most biomacromolecule-based bioinks: printed objects are difficult to maintain for prolonged storage without significant geometric deformation. The printed hydrogels typically shrink in dry environments due to dehydration and swell in moist environments due to water absorption. While radical scavenging improves printing precision, it is insufficient to prevent post-printing deformation, underscoring the need for additional structural regulation mechanisms. SF can be physically induced to form β-sheets owing to its unique chemical structure, offering a practical approach to address this issue. Herein, we evaluated the anti-swelling effect of alcohol on SF-containing hydrogels. As shown in **Fig. 2a**, PEGDA/CSMA/SF hydrogels were immersed in different concentrations of alcohol (50%, 80%, and 100%) for one hour, and the volume expansion ratios were about 146.4%, 92.4%, and 58.9%. After being immersed in deionized water for 24 h, the volume of the hydrogel without alcohol treatment increased by about 366.6%, whereas that of the hydrogel with alcohol (50%, 80%, and 100%) treatment increased by about 178.4%, 136.6%, and 116.8%, respectively. It was revealed that the PEGDA/CSMA/SF hydrogel swelled quickly in deionized water, and the anti-swelling effect of a low-concentration alcohol (50%) treatment was limited. In contrast, 100% alcohol treatment led to a significant reduction in volume, which was also unacceptable for the required precise assembly structures of 3D printing hydrogels. The treatment of immersing in 80% alcohol was satisfactory to prevent the hydrogel from shape changing significantly. Thus, we selected 80% alcohol treatment for the following anti-swelling experiments. We assessed the effect of alcohol treatment time on anti-swelling properties (**Fig. 2b**). It still showed noticeable swelling (about 233.6%) after 24 h rehydration with a 0.5 h treatment time. Treatments immersed in 80% alcohol for 1 and 2 hours reduced the volume swelling rate to about 143.3% and 138.8%, respectively. These results revealed that a PEGDA/CSMA/SF hydrogel treated with 80% alcohol for 1 h was an effective anti-swelling agent, preventing deformation of the geometric structure. Further, we measured the anti-swelling property of the 80% alcohol-treated PEGDA/CSMA/SF hydrogel immersed in deionized water for 72 h (**Fig. 2c**). The volume expansion ratio of the PEGDA/CSMA/SF hydrogel without treatment was about 366.5% over 72 h. The anti-swelling treatment resulted in a low swelling ratio (about 144.6%). We assessed the effect of alcohol-induced SF β-sheet formation on the hydrogel's mechanical properties through compressive tests (**Fig. 2d**).

We observed a significant enhancement in mechanical strength after our alcohol treatment (**Fig. 2e** and **2f**). The compressive modulus (10%-20% strain) of the initial PEGDA/CSMA/SF hydrogel was about 15.3 kPa, decreasing to about 9.5 kPa after immersion in water for 24 h. And the compressive modulus of alcohol-induced PEGDA/CSMA/SF hydrogel increased to 208.1 kPa, indicating that the SF-containing hydrogel can adjust the mechanical strength by inducing β-sheet formation to adapt to more application fields. Rapid swelling and inadequate mechanical strength represent pervasive issues for DLP 3D printed hydrogels. Although alcohol inducing treatment cannot enhance swelling resistance or mechanical strength during the printing process, nor was it suitable for cell-laden bioprinting, it offered a facile strategy for high-performance SF-containing DLP 3D printed hydrogels. We further studied the chemical structure of alcohol-induced PEGDA/CSMA/SF hydrogel by the FTIR spectrum at the range of 1800-1400 cm^{-1} (**Fig. 2g**). The amide I band shifted from 1651 to 1643 cm^{-1}, and the amide II band shifted from 1537 to 1517 cm^{-1}, demonstrating the transition of SF secondary conformation from random coils to β-sheets [37]. We also observed that alcohol inducement decreased the pore size of PEGDA/CSMA/SF hydrogel (from ~78.3 to ~23.6 μm) (**Fig. 2h**). Furthermore, the alcohol-treated PEGDA/CSMA/SF hydrogel exhibited a substantially slower degradation rate, retaining about 61.4% of its initial mass on the 21st day (**Fig. A1**). These results revealed that alcohol treatment could prevent volume swelling, enhance mechanical strength, decrease pore size, and suppress degradation by inducing SF β-sheet formation.

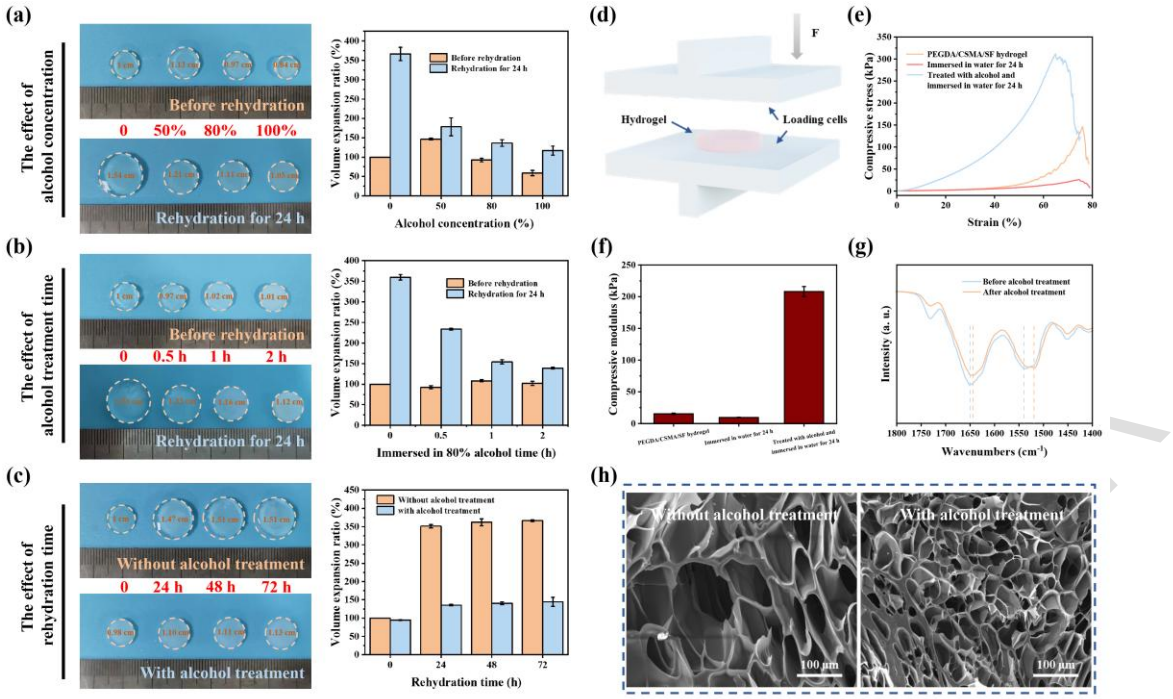

Figure 2. **The effect of alcohol inducing treatment on the PEGDA/CSMA/SF hydrogel**. The effects of alcohol concentration **(a)**, treatment time **(b)**, and rehydration time **(c)** on the anti-swelling performance (n = 3). Schematic diagram of compressive tests **(d)**. Stress/strain curves **(e)** and compressive modulus **(f)** of the hydrogels. Characteristic FTIR shift of amide I and II bands **(g)** and SEM images **(h)** after alcohol treatment.

As a material for promoting skin wound healing, its antibacterial properties are also a crucial consideration. *Escherichia coli* (*E. coli*) and *Staphylococcus aureus* (*S. aureus*) were selected as representative strains of Gram-negative and Gram-positive bacteria, respectively. The hydrogels were co-cultured with the bacteria, and optical density (OD) was measured to evaluate antibacterial activity. The antibacterial effect of PEGDA, CSMA, SF, and PEGDA/CSMA/SF against *E. coli* was about 2.67%, 46.6%, 0%, and 41.3% in 12 h, and that against *S. aureus* was about 1.2%, 48.4%, 4.2%, and 45.8% in 12 h (**Fig. 3a** and **3b**). The analysis of the antibacterial efficacy of PEGDA/CSMA/SF bioink components revealed that CSMA was the source of the activity. We employed the dilution spread-plate method to further confirm the antibacterial properties of PEGDA/CSMA/SF (**Fig. 3c**). The antibacterial properties of PEGDA/CSMA/SF suggested its potential as a bioink for skin wound treatment, but it had not been proven for treating established infections.

The bioink formulation design must incorporate biocompatibility as a critical requirement, and we selected bone marrow stromal cells (BMSCs) to assess the bioink hydrogels' biocompatibility *in vitro*. BMSCs proliferation exhibited minimal change during the 7-day co-cultured period with PEGDA/CSMA and PEGDA/CSMA/SF bioink hydrogels (**Fig. 3d**). We also conducted the Live/Dead staining to investigate the cytotoxicity (read dots for dead cells and green dots for live cells) (**Fig. 3e**). BMSCs co-cultured with bioink hydrogels exhibited comparable viability to the control group. These results revealed that SF was used to enhance the precision of DLP 3D printing without compromising cell viability. Moreover, BMSCs are co-cultured with the equal volume of alcohol-induced PEGDA/CSMA/SF bioink hydrogels, and the result showed that the alcohol-treated hydrogels took no detrimental effect on cell proliferation (**Fig. A2**).

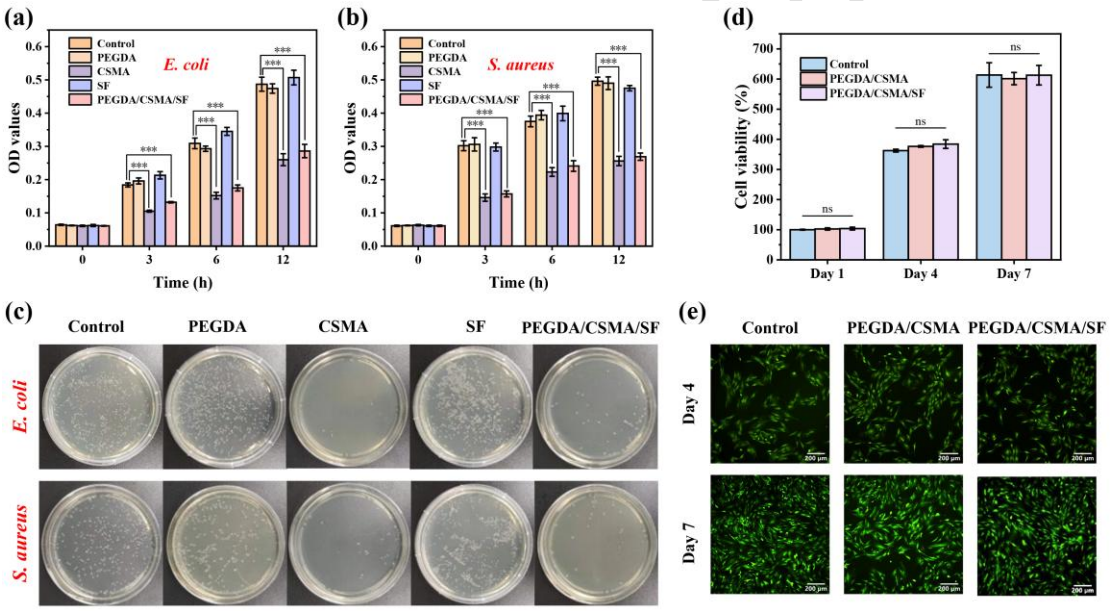

Figure 3. **The *in vitro* antibacterial activities and biocompatibility of the bioinks**. The OD values of *E. coli* **(a)** and *S. aureus* **(b)** treated with the bioinks for 3, 6, and 12 h. Photographs of bacterial colonies **(c)**. Cell viability **(d)** and Live/Dead assay images **(e)** of BMSCs co-cultured with the bioink hydrogels. (Mean ± SD, n = 6, *p < 0.05, **p < 0.01, ***p < 0.001).

The attenuation of the UV light intensity emitted by a single micromirror in a DLP printer from the center to the edge follows a Gaussian curve [38,39]. Besides exponential absorption dominated by the Beer–Lambert law, beam reflection and refraction would also occur when it penetrates the bioink [40]. It led to the formation of a parabolic-like cured zone, inconsistent with

the theoretical UV intensity distribution. As shown in **Fig. 4a**, the vertical resolution was dominated by cured depth (R_d), and the lateral resolution was dominated by cured width (R_w). Light scattering expanded the cured vertical area, and SF could counteract this effect by inhibiting excessive free-radical reactions. The mechanism by which SF participates in the bioink photopolymerization reaction is shown in **Fig. 4b**. Firstly, the polymerization reaction was initiated by free radicals generated from LAP under UV irradiation. The free radicals attacked the double bonds of PEGDA and CSMA, as well as the phenolic groups of SF. The free-radical-activated PEGDA and CSMA further advanced chain propagation, and we hypothesized that activated SF directly participated in chain termination, preventing runaway polymerization. The capacity of SF to bind free radicals was also verified. As shown in **Fig. 4c** and **4d**, SF could scavenge DPPH about 55.1% in 6 h and inhibit H_2O_2 about 33.6% in 24 h. The concentrations of DPPH and H_2O_2 also decreased slightly in the PEGDA/CSMA and PEGDA/CSMA/SF hydrogel groups, due to the hydrogels' absorption effects. **Fig. 4e** showed SF's capacity to inhibit H_2O_2 over time, with an effect of about 68.2% after 48 h. These results demonstrated that SF possessed the free-radical-scavenging potential to enhance 3D printing precision. The DLP 3D printer fabricated printouts by curing bioink layer upon layer, so that monolayer printing fidelity could serve as an indicator of the precision of complex multilayer objects. We adopted a spoke-like pattern, initially proposed by You et al. [40], with a monolayer of 100 μm to evaluate the effect of SF on 3D printing fidelity by calculating the ratio of cured area (marked with a red circle) and designed area (marked with a yellow circle) (**Fig. 4f**). It was evident that PEGDA/CSMA/SF bioink exhibits superior printability. There was about 1.29% unresolved region in the PEGDA/CSMA/SF group, and about 63.01% unresolved region in the PEGDA/CSMA group. It also demonstrated that even relatively simple structures required polymerization inhibitors to achieve high-fidelity printing. Moreover, we fabricated hydrogel scaffolds with 1 mm square pore structures (**Fig. 4g**). The PEGDA/CSMA/SF bioink yielded well-resolved structures and was employed in subsequent animal experiments.

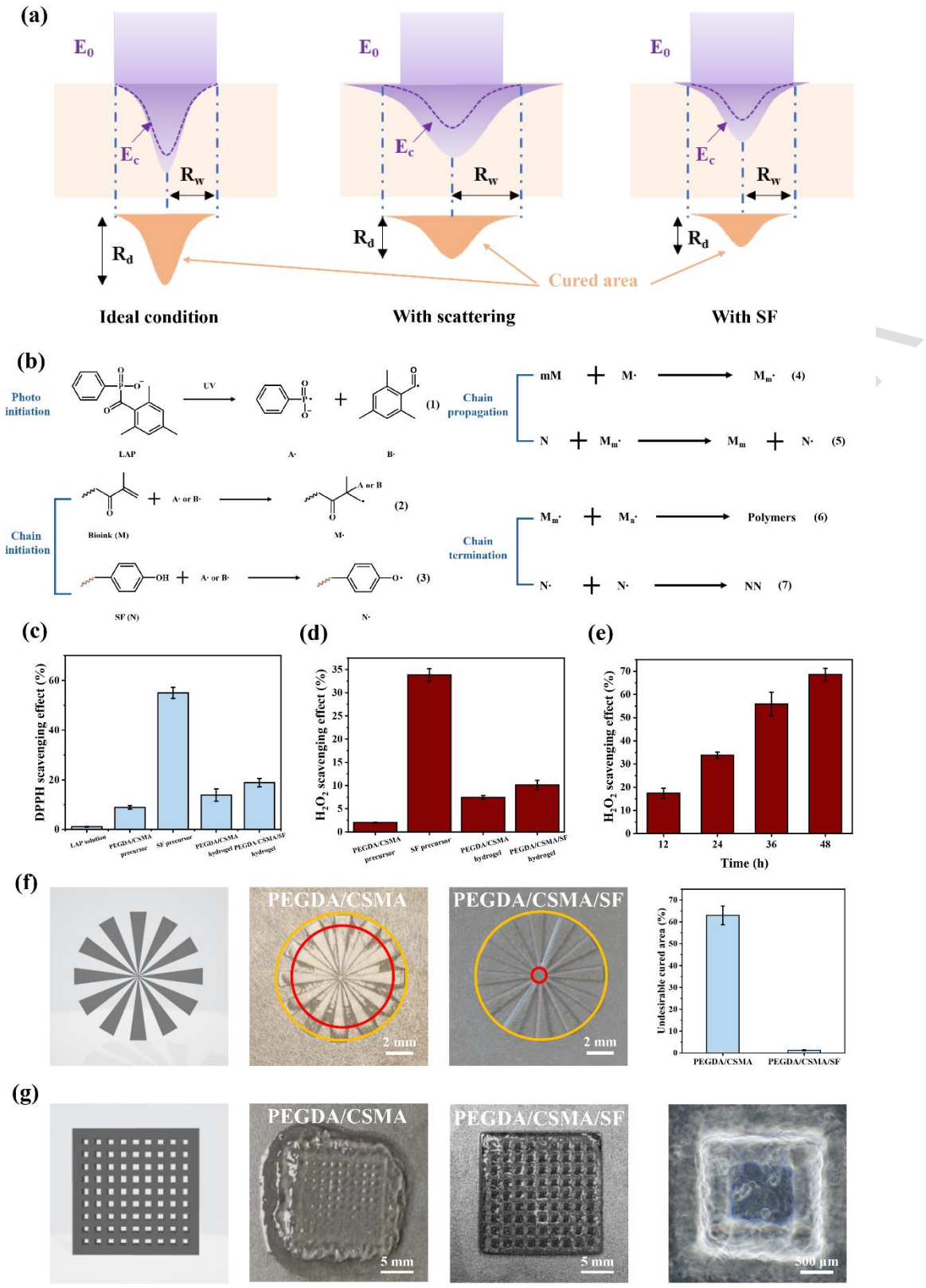

Figure 4. SF enhances 3D printing precision. Schematic diagram illustrating the Gaussian beam intensity profile and cured area in different scenarios, E_0 for the light intensity at the bioink surface, E_c for the critical energy required to initiate polymerization, R_d and R_w for the

curing depth and width, respectively **(a)**. The mechanism of PEGDA/CSMA/SF polymerization **(b)**. The capacity of SF scavenging DPPH **(c)** and HO· free radicals **(d**, **e)**. The printed spoke-like pattern to evaluate the printing fidelity: Solidworks model, the printed hydrogels with PEGDA/CSMA and PEGDA/CSMA/SF bioinks (yellow circles for designed area and red circles for unresolved area), the unresolved area ratios (from left to right) **(f)**. The porous hydrogel scaffold Solidworks model, printed with PEGDA/CSMA, printed with PEGDA/CSMA/SF, and the micrograph of the pores (from left to right) **(g)**.

In the *in vivo* skin defect repair model, we monitored the healing process daily, and the healing performance was shown in **Fig. 5a** and **5b**. All hydrogel groups and the control group exhibited reduced wound areas within 14 days. On the 7th day, the wound area of the control group was about 0.366 cm^2, and that of the PEGDA/CSMA hydrogel group was about 0.196 cm^2. The therapeutic effect was mainly attributed to the bioactivity of CSMA, which stimulated fibroblast and keratinocyte proliferation and migration [41]. Compared with the PEGDA/CSMA hydrogel, the PEGDA/CSMA/SF hydrogel exhibits enhanced wound-healing effects. There was a very tiny wound area in the PEGDA/CSMA/SF hydrogel group on the 14th day. It was attributed to a range of biological functions of SF, such as promoting cell adhesion and proliferation [42], inducing pro-regenerative macrophages and recruiting hair follicle stem cells [43], and immunoregulation [44]. Notably, PEGDA/CSMA/SF scaffold treatment yielded more efficient wound repair than PEGDA/CSMA/SF hydrogel treatment. Because the printed porous structure prevented hypoxic conditions at the wound site, and facilitated cell migration, infiltration, and angiogenesis [45]. We performed H&E staining on tissue samples to investigate the wound-healing process. On the 3rd day, tissues exhibited predominant inflammatory exudation and infiltration of inflammatory cells in all groups, consistent with the inflammatory phase. On the 7th day, extensive inflammatory cell infiltration remains in the control group, and complete thin epithelial layers were observed in the PEGDA/CSMA/SF hydrogel and scaffold groups. Moreover, the proliferative activity of granulation tissue and fibroblasts peaked at this stage. It was observed that PEGDA/CSMA/SF scaffold group achieved the highest level of re-epithelialization, angiogenesis, and collagen fiber formation on the 14th day.

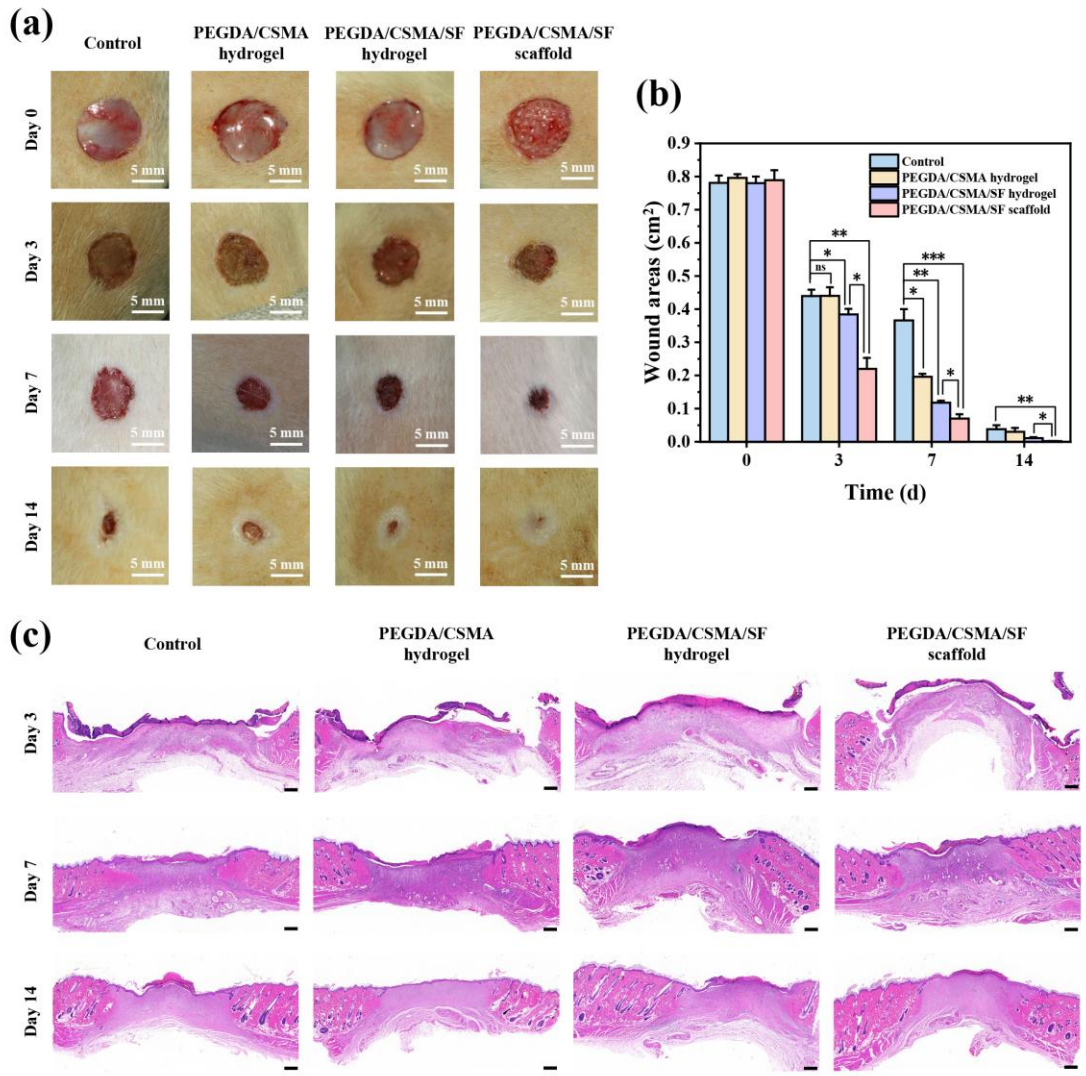

Figure 5. **Wound healing performance of the bioinks on full-thickness skin defects**. The representative photographs of the skin wound **(a)**. Quantitative analysis of the wound area (Mean ± SD, n = 6, *p < 0.05, **p < 0.01, ***p < 0.001) **(b)**. H&E staining images of the tissue samples (scale bar: 500 μm) **(c)**.

Collagen formation and orderly alignment are critical to skin wound healing, and we conducted Masson staining to analyze collagen fiber deposition (**Fig. 6a**, left). The collagen volume fractions were measured at about 29.68%, 35.55%, 46.65%, and 52.07% in the group of control, PEGDA/CSMA hydrogel, PEGDA/CSMA/SF hydrogel, and PEGDA/CSMA/SF scaffold on the 3rd day, respectively (**Fig. 6b**). It reveals that the traditional PEGDA/CSMA hydrogel promotes collagen deposition. The incorporation of SF, along with a more rational spatial architecture, significantly heightens this effect. We marked the mature blood vessels of

the skin tissue samples with CD31 (**Fig. 6a**, right) (red arrows for mature blood vessels), and the corresponding quantitative information is exhibited in **Fig. 6c**. The vascular composition in the control group is characterized by a predominance of immature vessels. PEGDA/CSMA/SF hydrogel and PEGDA/CSMA/SF scaffold groups both exhibit higher CD31 expression and a substantial number of mature blood vessels, indicating that SF promotes angiogenesis in wound healing.

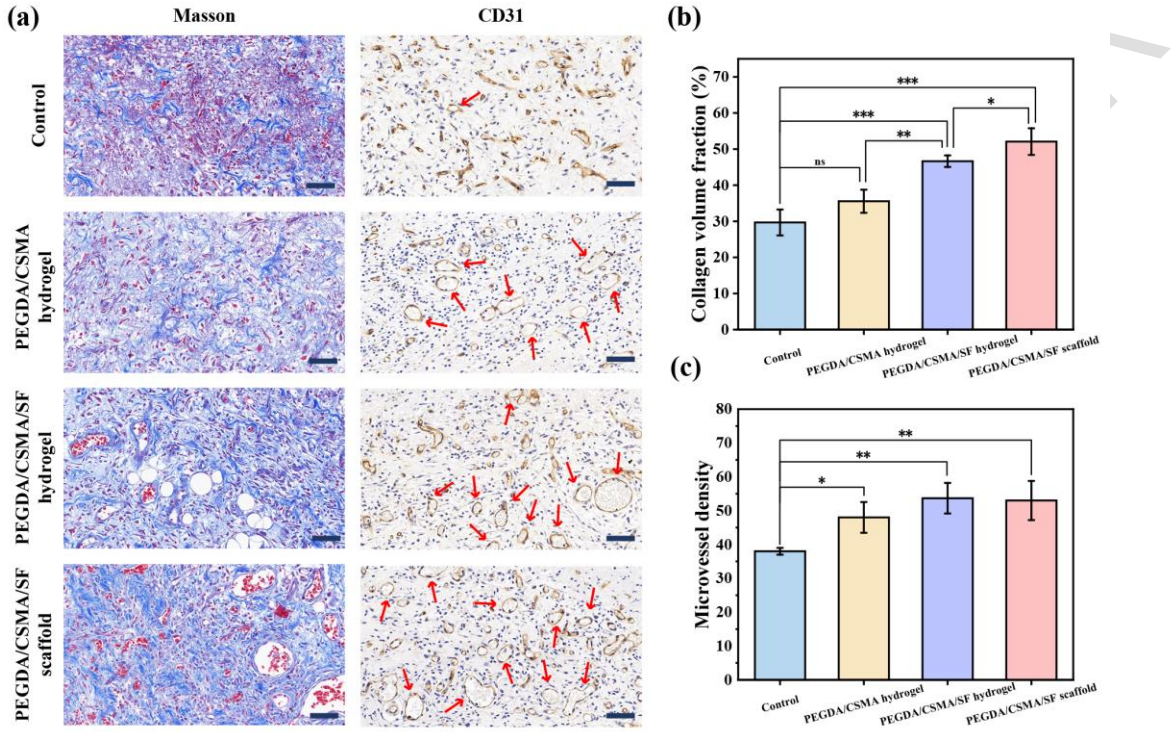

Figure 6. **Immunohistochemical analysis of wound healing**. Masson staining images (left) and CD31 expression (right) on the 3rd day (scale bar: 50 μm) **(a)**. The collagen volume fraction on the 3rd day **(b)**. The microvessel density presented by CD31 on the 3rd day **(c)**. (Mean ± SD, n = 6, *p < 0.05, **p < 0.01, ***p < 0.001).

Vascular endothelial growth factor (VEGF) plays a critical and multifunctional role in skin wound repair by promoting angiogenesis, recruiting inflammatory cells, enhancing collagen deposition, and accelerating re-epithelialization [46]. As shown in **Fig. 7a** (left) and **7b**, VEGFA expression was significantly upregulated in SF-containing groups, and the PEGDA/CSMA/SF scaffold with the rationally designed architecture was superior to the traditional PEGDA/CSMA/SF hydrogel dressing in promoting VEGFA expression. Tumor necrosis factor (TNF) is a concentration-dependent factor in skin therapy: a necessary inflammatory signal at

low levels and a tissue-destructive factor at high levels. The expression of TNF-α was exhibited in **Fig. 7a** (right) and **7c**. Compared with the control group, TNF-α expression was lower in the other hydrogel-treated groups. Moreover, the more pronounced suppression of TNF-α expression observed in SF-containing groups indicated the effect of SF on down-regulating TNF-α.

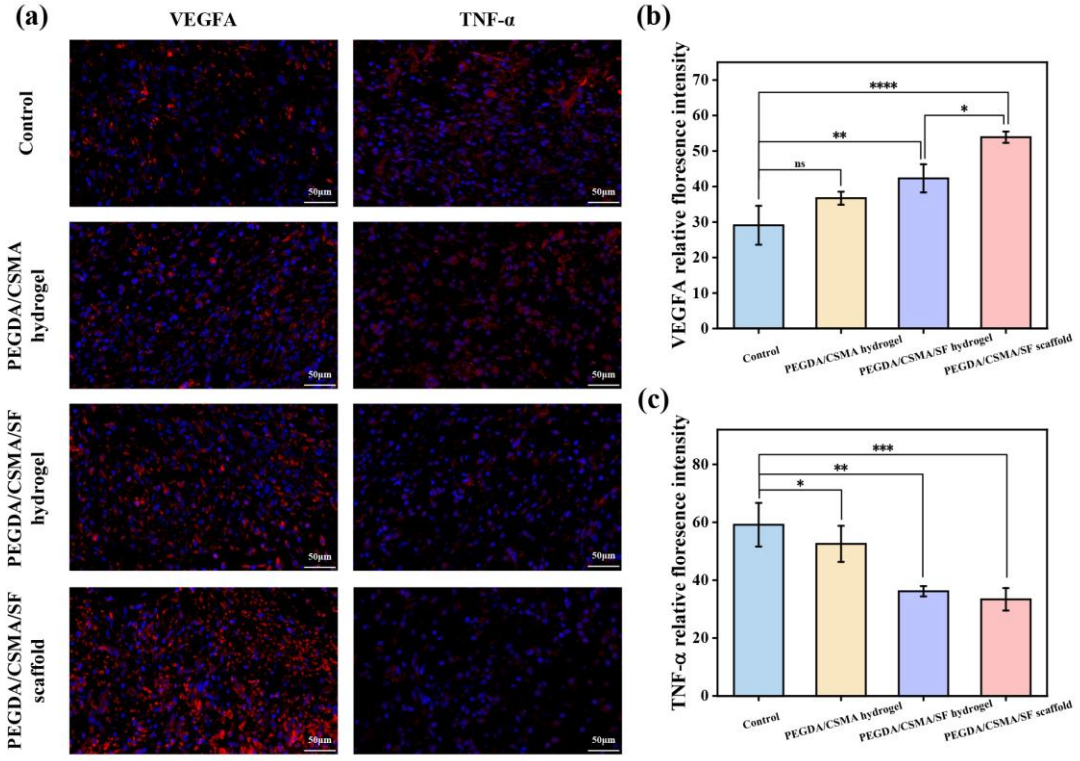

Figure 7. **Immunofluorescence staining analysis of wound healing**. Representative images of skin tissue sections on the 3rd day after immunofluorescence staining labeling with VEGFA (left) and TNF-α (right) (scale bar: 50 μm) **(a)**. Quantified analysis of VEGFA **(b)** and TNF-α **(c)**. (Mean ± SD, n = 6, *p < 0.05, **p < 0.01, ***p < 0.001).

4. Conclusion

In this work, we introduced SF, a phenol-containing natural macromolecule protein, into the traditional DLP 3D printing PEGDA/CSMA bioink to enhance the printing accuracy. This effect primarily relied on SF's moderate free-radical-scavenging ability to suppress runaway photo-polymerization during the printing process. Compared with previous strategies that focused solely on polymerization control, this work demonstrated that integrating radical

regulation with network stabilization was essential for achieving functional, structurally stable 3D-printed constructs. We explored the alcohol inducing treatment to enhance the mechanical performance and suppress the swelling ratio of the cell-free PEGDA/CSMA/SF hydrogels via β-sheet formation. The volume swelling ratio of untreated PEGDA/CSMA/SF hydrogel immersed in water for 24 h was about 366.5%, and that of alcohol-treated and rehydrated samples exhibited a sharp reduction to about 138.8%. It was accompanied by a substantial increase in the compressive modulus from about 9.5 kPa to 208.1 kPa. PEGDA/CSMA/SF bioink hydrogel exhibited satisfactory resistance against *E. coli* and *S. aureus*, along with outstanding biocompatibility. We printed porous scaffolds with the PEGDA/CSMA/SF bioink, and *in vivo* experiments revealed that the hydrogel scaffolds could accelerate skin wound healing by promoting collagen deposition and angiogenesis, upregulating VEGFA expression, and downregulating TNF-α expression. Integrating SF into traditional bioinks provides a straightforward and robust strategy with considerable potential for DLP 3D bioprinting applications in biological repair. Furthermore, alcohol-induced treatment significantly enhances the mechanical properties and swelling resistance of 3D printed hydrogels, thereby supporting the further applications in wet physiological environments and load-bearing sites *in vivo*. However, it is noted that the cytotoxicity of alcohols associated with this treatment precludes its direct application in cell-laden hydrogel scaffolds. The exploration of a mild and cytocompatible induction strategy holds significant research value. An additional limitation lies in the fact that the skin defect has not been analyzed at multiple time points, leading to inadequate explanation of the dynamic mechanisms of wound healing.

Funding

This research was supported by the Natural Science Foundation of Zhejiang Province (LZ25H060001)

Conflict of interest

Wei Wei is an Editorial Board Member of this journal, but was not in any way involved in the

editorial and peer-review process conducted for this paper, directly or indirectly. The authors declare no competing interests.

Author contributions

Conceptualization: Xinrang Zhai

Formal analysis: Miner Hu

Funding acquisition: Wei Dong, Jianjun Ma, Wei Wei

Investigation: Xinrang Zhai, Linran Song

Project administration: Wei Dong, Jianjun Ma, Wei Wei

Supervision: Wei Dong, Jianjun Ma, Wei Wei

Writing–original draft: Xinrang Zhai

Ethics approval and consent to participate

All animal procedures were performed in accordance with the guidelines approved by the Zhejiang University Ethics Committee (Ethical NO. ZJU202550988).

Consent for publication

Not applicable.

Availability of data

Original data are available from the corresponding authors upon reasonable request. This paper does not report original code. Any additional information required to reanalyze the data reported in this paper is available from the lead contact upon request.

References

1. Wang Q., Liu Y., Zhang S., et al. Exosome-based bioinks for 3D bioprinting applications in tissue engineering and regenerative medicine. *Int. J. Bioprint*. 2023; 9(6): 0114. doi:10.36922/ijb.0114

2. Yu W., Liu X., Liu Y., Chen X., Ge S., Dong Z.. 3D printing of phase-separating hydrogels with tunable microachitecture for mechanoregulated bone regeneration. *Adv. Funct. Mater*. 2025; 36(30): e23349. doi:10.1002/adfm.202523349

3. Andreu A., Lee H., Kang J., Yoon Y.J.. Self-healing materials for 3D printing. *Adv. Funct. Mater*. 2024; 34(30): 2315046. doi:10.1002/adfm.202315046

4. Elder B., Neupane R., Tokita E., Ghosh U., Hales S., Kong Y.L.. Nanomaterial patterning in 3D printing. *Adv. Mater*. 2020; 32(17): 1907142. doi:10.1002/adma.201907142

5. Pal S., Gavhane U.A., S. K A.. Biocompatible PVAc-g-PLLA acrylate polymers for DLP 3D printing with tunable mechanical properties. *ACS Appl. Mater. Interfaces*. 2024; 16(45): 62594-62605. doi:10.1021/acsami.4c11285

6. Zhang N., Lu Y., Li J., et al. DLP 3D printing of hyperelastic photocurable perivascular scaffolds enabling patient-specific vascular remodeling. *Acta Biomater*. 2025; 203: 381-398. doi:10.1016/j.actbio.2025.07.048

7. Xu Z., Zhang Q., Fan C., et al. A gel microparticle-based self-thickening strategy for 3D printing high-modulus hydrogels skeleton cushioned with PNAGA hydrogel mimicking anisotropic mechanics of meniscus. *Bioact. Mater*. 2023; 26: 64-76. doi:10.1016/j.bioactmat.2023.02.020

8. Yang X,. Yao L., Sun X., Wang L., Xiao J.. Low-temperature DLP 3D printing of low-concentration collagen methacryloyl for the fabrication of durable and bioactive personalized scaffolds. *Chem. Eng. J*. 2024; 497: 155650. doi:10.1016/j.cej.2024.155650

9. Yuan H., Xiao P., Sarmento B., Chen G., Cui W.. Synovial lubrication factors-recruiting biomimetic polyphenolized hyaluronic acid for promoting cartilage repair. *Adv. Funct. Mater*. 2024; 34: 2406668. doi:10.1002/adfm.202406668

10. Hong H., Seo Y.B., Kim D.Y., et al. Digital light processing 3D printed silk fibroin hydrogel for cartilage tissue engineering. *Biomaterials* 2020; 232: 119679.

doi:10.1016/j.biomaterials.2019.119679

11. Ye J., Li F., Wen Z., et al. Multichannel 3D-printed bioactive scaffold combined with small interfering RNA delivery to promote neurological recovery after spinal cord injury. *Research* 2025; 8: 0961. doi:10.34133/research.0951

12. Na K., Shin S., Lee H., et al. Effect of solution viscosity on retardation of cell sedimentation in DLP 3D printing of gelatin methacrylate/silk fibroin bioink. *J. Ind. Eng. Chem*. 2018; 61: 340-347. doi:10.1016/j.jiec.2017.12.032

13. He Y., Wang F., Wang X., Zhang J., Wang D., Huang X.. A photocurable hybrid chitosan/acrylamide bioink for DLP based 3D bioprinting. *Mater. Des*. 2021; 202: 109588. doi:10.1016/j.matdes.2021.109588

14. Yang M., Chu L., Zhuang Y., et al. Multi-material digital light processing (DLP) bioprinting of heterogeneous hydrogel constructs with perfusable networks. *Adv. Funct. Mater*. 2024; 34(32): 2316456. doi:10.1002/adfm.202316456

15. Wei Q., Liu D., Chu G., et al. TGF-β1-supplemented decellularized annulus fibrosus matrix hydrogels promote annulus fibrosus repair. *Bioact. Mater*. 2023; 19: 581-593. doi:10.1016/j.bioactmat.2022.04.025

16. Li X., Xing R., Xu C., et al. Immunostimulatory effect of chitosan and quaternary chitosan: A review of potential vaccine adjuvants. *Carbohydr. Polym*. 2021; 264: 118060. doi:10.1016/j.carbpol.2021.118050

17. Rezaei F.S., Sharifianjazi F., Esmaeilkhanian A., Salehi E.. Chitosan films and scaffolds for regenerative medicine applications: A review. *Carbohydr. Polym*. 2021; 273: 118631. doi:10.1016/j.carbpol.2021.118631

18. Zanon M., Cue-López R., Martínez-Campos E., et al. Bioderived dyes-mediated vat photopolymerization 3D printing of chitosan hydrogels for tissue engineering. *Addit. Manuf*. 2023; 69: 103553. doi:10.1016/j.addma.2023.103553

19. Cheng F., Zhang X., Dai J., et al. Digital light processing-printed nanozyme-integrated hydrogels enable spatiotemporal immunomodulation and repair of infected wounds. *Acta Biomater*. 2026; 214: 254-270. doi:10.1016/j.actbio.2026.03.013

20. Shen Y., Tang H., Huang X., et al. DLP printing photocurable chitosan to build bio-constructs for tissue engineering. *Carbohydr. Polym*. 2020; 235: 115970.

doi:10.1016/j.carbpol.2020.115970

21. Miri A.K., Nieto D., Iglesias L., et al. Microfluidics-enabled multimaterial maskless stereolithographic bioprinting. *Adv. Mater*. 2018; 30(27): 1800242. doi:10.1002/adma.201800242

22. He N., Wang X., Shi L., et al. Photoinhibiting via simultaneous photoabsorption and free-radical reaction for high-fidelity light-based bioprinting. *Nat. Commun*. 2023; 14(1): 3063. doi:10.1038/s41467-023-38838-2

23. Ma Y., Wei W., Gong L., et al. Biomacromolecule-based agent for high-precision light-based 3D hydrogel bioprinting. *Cell Rep. Phys. Sci*. 2022; 3(8): 100985. doi:10.1016/j.xcrp.2022.100985

24. Zhan Y., Fu W., Xing Y., Ma X., Chen C.. Advances in versatile anti-swelling polymer hydrogels. *Mater. Sci. Eng. C* 2021; 127: 112208. doi:10.1016/j.msec.2021.112208

25. Pan X., Li R., Li W., et al. Silk fibroin hydrogel adhesive enables sealed-tight reconstruction of meniscus tears. *Nat. Commun*. 2024; 15(1): 2651. doi:10.1038/s41467-024-47029-6

26. Kundu B., Rajkhowa R., Kundu S.C., Wang X. Silk fibroin biomaterials for tissue regenerations. *Adv. Drug Delivery Rev*. 2013; 65(4): 457-470. doi:10.1016/j.addr.2012.09.043

27. Fei Y., Wang X., Ling Z., et al. Angiogenic apoptotic vesicle-laden silk fibroin /sodium alginate hydrogel for pulp regeneration. *Mater. Today Bio* 2025; 33: 102060. doi:10.1016/j.mtbio.2025.102060

28. Wu D., Li J., Wang C., et al. Injectable silk fibroin peptide nanofiber hydrogel composite scaffolds for cartilage regeneration. *Mater. Today Bio* 2024; 25: 100962. doi:10.1016/j.mtbio.2024.100962

29. Su D., Yao M., Liu J., Zhong Y., Chen X., Shao Z.. Enhancing mechanical properties of silk fibroin hydrogel through restricting the growth of β-sheet domains. *ACS Appl. Mater. Interfaces* 2017; 9(20): 17489-17498. doi:10.1021/acsami.7b04623

30. Hasturk O., Jordan K.E., Choi J., Kaplan D.L.. Enzymatically crosslinked silk and silk-gelatin hydrogels with tunable gelation kinetics, mechanical properties and bioactivity for cell culture and encapsulation. *Biomaterials* 2020; 232: 119720. doi:10.1016/j.biomaterials.2019.119720

31. Kaewpirom S., Teangtam W., Monthatong M., Boonsang S.. Modification of silk fibroin film structure: From silkworm diet to material properties. *Int. J. Biol. Macromol*. 2025; 317: 144855. doi:10.1016/j.ijbiomac.2025.144855

32. Li H., Ma T., Zhang J., et al. Boosting corrosion resistance and osteogenic activity of magnesium-based implants with metal ions chelated silk fibroin coating via binary solvent system. *Chem. Eng. J*. 2024; 485: 149905. doi:10.1016/j.cej.2024.149905

33. Rockwood D.N., Preda R.C., Yücel T., Wang X., Lovett M.L., Kaplan D.L.. Materials fabrication from Bombyx mori silk fibroin. *Nat. Protoc*. 2011; 6(10): 1612-1631. doi:10.1038/nprot.2011.379

34. Hu H., Zhai X., Li W., et al. A photo-triggering double cross-linked adhesive, antibacterial, and biocompatible hydrogel for wound healing. *iScience* 2022; 25(7): 104619. doi:10.1016/j.isci.2022.104619

35. Zhang X., Yang D., Nie J.. Chitosan/polyethylene glycol diacrylate films as potential wound dressing material. *Int. J. Biol. Macromol*. 2008; 43(5): 456-462. doi:10.1016/j.ijbiomac.2008.08.010

36. Zhai X., Hu M., Song L., et al. Silk fibroin based bioinks for high-precision digital light processing 3D printing. *Int. J. Biol. Macromol*. 2025; 310: 143248. doi:10.1016/j.ijbiomac.2025.143248

37. Wang H., Zhang Y., Shao H., Hu X.. A study on the flow stability of regenerated silk fibroin aqueous solution. *Int. J. Biol. Macromol*. 2005; 36(1-2): 66-70. doi:10.1016/j.ijbiomac.2005.03.011

38. Yu K., Zhang X., Sun Y., et al. Printability during projection-based 3D bioprinting. *Bioact. Mater*. 2022; 11: 254-267. doi:10.1016/j.bioactmat.2021.09.021

39. Zakeri S., Vippola M., Levänen E.. A comprehensive review of the photopolymerization of ceramic resins used in stereolithography. *Addit. Manuf*. 2020; 35: 101177. doi:10.1016/j.addma.2020.101177

40. You S., Wang P., Schimelman J., Hwang H.H., Chen S.. High-fidelity 3D printing using flashing photopolymerization. *Addit. Manuf*. 2019; 30: 100834. doi:10.1016/j.addma.2019.100834

41. Priya S., Choudhari M., Tomar Y., et al. Exploring polysaccharide-based bio-adhesive

topical film as a potential platform for wound dressing application: A review. *Carbohydr. Polym*. 2024; 327: 121655. doi:10.1016/j.carbpol.2023.121655

42. Kulkarni G., Guha Ray P., Byram P.K., Kaushal M., Dhara S., Das S.. Tailorable hydrogel of gelatin with silk fibroin and its activation/crosslinking for enhanced proliferation of fibroblast cells. *Int. J. Biol. Macromol*. 2020; 164: 4073-4083. doi:10.1016/j.ijbiomac.2020.09.016

43. Liang R., Shen X., Xie C., et al. Silk gel recruits specific cell populations for scarless skin regeneration. *Appl. Mater. Today* 2021; 23: 101004. doi:10.1016/j.apmt.2021.101004

44. Chen Z., Cheng J., Wang M., et al. In situ forming silk fibroin hydrogel dressing accelerates acute wound healing via immunomodulation and extracellular matrix regeneration. *J. Controlled Release* 2025; 387: 114228. doi:10.1016/j.jconrel.2025.114228

45. Guan Q., Hou S., Wang K., et al. Micropore structure engineering of injectable granular hydrogels via controlled liquid-liquid phase separation facilitates regenerative wound healing in mice and pigs. *Biomaterials* 2025; 318: 123192. doi:10.1016/j.biomaterials.2025.123192

46. Tetik-Elsherbiny N., Elsherbiny A., Setya A., et al. RNF20-mediated transcriptional pausing and VEGFA splicing orchestrate vessel growth. *Nat. Cardiovasc. Res*. 2024; 3(10): 1199-1216. doi:10.1038/s44161-024-00546-5

Appendix

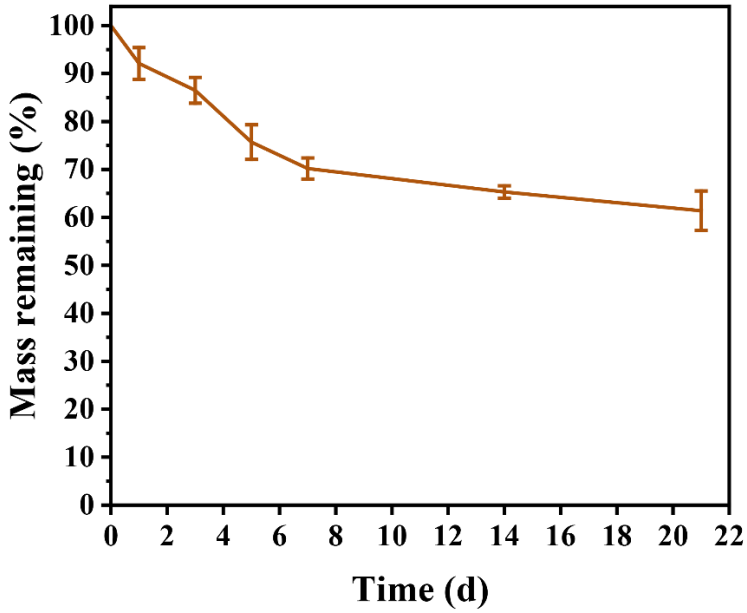

Figure A1. The degradation behavior of the alcohol-induced PEGDA/CSMA/SF hydrogel.

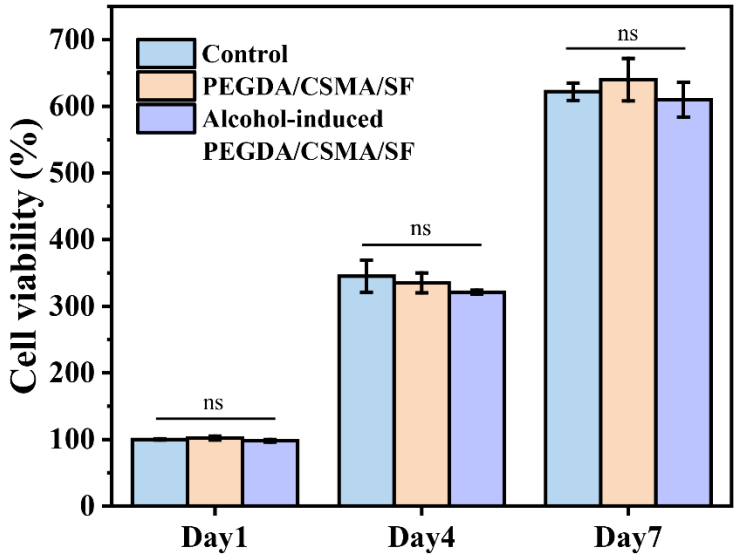

Figure A2. Cell viability of BMSCs co-cultured with PEGDA/CSMA/SF and alcohol-induced hydrogels.